Available online at www.sciencedirect.com
ScienceDirect
Journal of the European Ceramic Society 31 (2011) 2119–2128
www.elsevier.com/locate/jeurceramsoc

ZnO and CuO crystal precipitation in sintering Cu-doped Ni–Zn ferrites. I. Influence of dry relative density and cooling rate

Antonio Barba *, Carolina Clausell, Juan Carlos Jarque, María Monzó

Instituto de Tecnología Cerámica, Asociación de Investigación de las Industrias Cerámicas, Universitat Jaume I, 12006 Castellón, Spain

Received 9 January 2011; received in revised form 26 April 2011; accepted 7 May 2011
Available online 31 May 2011

Abstract

This paper presents a study of the precipitation of ZnO and CuO crystals during the sintering of Cu-doped Ni–Zn ferrites. The nature of the Zn- and Cu-containing crystal precipitates was determined by scanning electron microscopy (SEM), energy-dispersive X-ray (EDX) analysis, X-ray diffraction (XRD), and X-ray photoelectron spectroscopy (XPS). The influence of the dry relative density of the body and the cooling rate on the occurring precipitates was also studied. Two consecutive chemical reactions are put forward, which explain the bulk precipitation of the zinc and copper oxides in the specimen during sintering, and their re-dissolution during cooling.

Keywords: Ferrites; Sintering; Precipitation; Zinc oxide; Copper oxide

1. Introduction

The ceramic powders generally known as ferrites are essentially mixed oxides of iron and one or more metallic elements. Ferrite powders containing nickel and zinc and different amounts of copper are typically used to mould bodies that prevent interference between electronic devices, given their electromagnetic wave absorption capacity.[1–4] The magnetic properties of these materials are not only determined by their chemical composition but also by their microstructure, i.e. grain- and pore-size distribution, total porosity (or relative density), and grain-boundary characteristics.[5–7]

Ferrites can be made by the conventional ceramic process, in which the main technological issues are: (i) obtaining bodies with high relative density (very low porosity); (ii) increasing grain size uniformly while maintaining a small average grain size and narrow grain-size distribution; and (iii) avoiding abnormal grain growth. In the case of Ni–Zn ferrites, the two principal variables controlling the sintering stage are peak sintering temperature and residence time at peak temperature.[7,8]

Previous papers by the present authors addressed the synthesis,[9] sintering,[10–16] and properties[17] of Cu-doped Ni–Zn ferrites. A thermal cycle, based on sintering kinetics, was also established[14–16] in order to sinter a ferrite of chemical composition $(Cu_{0.12}Ni_{0.23}Zn_{0.65})Fe_2O_4$. Crystal precipitates were detected on grain boundaries in certain sintered bodies, the occurring precipitates depending on dry relative density, peak sintering temperature, sintering time, and cooling rate. This behaviour had already been observed when non-doped Ni–Zn ferrites were sintered.[18–20] Those researchers concluded that ZnO could precipitate under certain sintering conditions, though no clear relationship between the sintering variables and the occurring crystal precipitates was obtained.

The present study was undertaken to determine the nature of the crystal precipitates that occurred during the sintering of Cu-doped Ni–Zn ferrites and to establish the relationship between their occurrence and two sintering variables (dry relative density and cooling rate), in order either to prevent crystal precipitates from forming during sintering or to dissolve the crystal precipitates in the cooling stage of the thermal cycle.

2. Experimental procedure

2.1. Material preparation

A spray-dried ferrite powder of approximate chemical composition $(Cu_{0.12}Ni_{0.23}Zn_{0.65})Fe_2O_4$, supplied by Fair-Rite

* Corresponding author. Tel.: +34 964 729 032; fax: +34 964 728 980.
E-mail address: barba@qui.uji.es (A. Barba).

0955-2219/$ – see front matter © 2011 Elsevier Ltd. All rights reserved.
doi:10.1016/j.jeurceramsoc.2011.05.007

Products Corp., was used as raw material. The true density of the ferrite powder was experimentally determined on a helium pycnometer to be 5380 kg/m^3.

The ferrite powder consisted of granules with an average size of 175 μm, made up of particles with an average size of 2.1 μm (and narrow particle-size distribution). The granules were used to form cylindrical test specimens, 3 mm thick and 2 cm in diameter, by uniaxial pressing at 50, 110, 120, 130, 140, and 300 MPa.

The specimens were sintered in air in an electric laboratory kiln using the following thermal cycle:

(1) Preheating stage (burnout of organic additives used in the compaction stage): heating at a rate of 12 °C/min to a peak temperature of 400 °C and 2-h dwell at this temperature.
(2) Densification and grain growth stage: heating at a rate of 12 °C/min to a peak sintering temperature of 1200 °C (hereafter termed sintering temperature) and 2-h dwell at this temperature (hereafter termed sintering time).
(3) Cooling stage: cooling from sintering to room temperature at three different cooling rates: fast cooling (the specimens were withdrawn from the kiln and left to cool at room temperature), and 20 and 0.5 °C/min.

Bulk density of the dry and sintered pieces was determined by the Archimedes method. The relative density (ϕ) of each ferrite specimen was calculated as the quotient of bulk density to true density.

2.2. Characterization

Each cylindrical sintered specimen was transversally cut to obtain a rectangular cross-section. The cross-sectional area was polished with diamond paste to a 1 μm finish and then subjected to thermal etching by heating at 100–120 °C below sintering temperature for 30 min, using a heating rate of 15 °C/min.[14] The cross-sectional area of the rectangular etched surface was then characterized. This was done as follows:

1. Specimen microstructure was observed in a scanning electron microscope (SEM).
2. The chemical composition was analysed by energy-dispersive X-ray (EDX) microanalysis, which enabled the average chemical composition of a given surface area or point chemical composition to be obtained.
3. The crystal structures were determined by X-ray diffraction (XRD).
4. The binding energy of the chemical bond for every chemical element, which depended on its coordination number (crystal field) and oxidation state, was determined by X-ray photoelectron spectroscopy (XPS) using non-monochromatic Al Kα radiation (1486.6 eV).

Table 1
Dry and sintered relative density of each specimen.

P (MPa)	Dry ϕ	Sintered ϕ		
		Fast cooling	Cooling at 20 °C/min	Cooling at 0.5 °C/min
50	0.527	0.915	0.908	0.906
110	0.573	0.943	0.940	0.940
120	0.578	0.946	0.941	0.940
130	0.583	0.950	0.944	0.943
140	0.587	0.950	0.944	0.944
300	0.624	0.961	0.961	0.958

3. Results and discussion

Specimen dry and sintered relative densities are shown in Table 1.

3.1. SEM results

Figs. 1–3 show the cross-sectional microstructure (SEM micrographs) of the specimens, with their outer and inner regions. Fig. 4 schematically illustrates the area occupied by the crystal precipitates at the tested dry relative densities and cooling rates. The white areas correspond to regions free of crystal precipitates, while the dotted areas correspond to regions occupied by crystal precipitates. The greater the dot density in the dotted area, the greater was the crystal density observed in the characterized sample. The micrographs allow the following conclusions to be drawn:

1. Certain ferrite sintering conditions gave rise to crystal precipitates. The detected crystals and crystal concentrations increased with the dry relative density and the cooling rate.
2. When the crystal concentrations increased, the crystals occurred, first, at triple joint points, then on grain boundaries and, finally (when the triple joint points and grain boundaries had been saturated), inside the ferrite grains.
3. The highest concentration of crystal precipitates was observed in the inner area, whereas the lowest concentration was located in the outer area, suggesting that the crystals had either precipitated from inside outwards or that the crystal precipitates had been removed, after precipitation, removal proceeding from the outer area inwards.
4. Rounded as well as needle-shaped crystal precipitates were observed: the first crystal precipitates were detected in the 0.573-dry relative density body and had a rounded shape, whereas needle-shaped crystal precipitates began to be detected when dry relative density increased. The needle-shaped precipitates were located around the rounded precipitates and, when the surfaces of the latter had been saturated, inside the ferrite grains.

The occurrence and cross-sectional distribution of the crystal precipitates are presumably to be explained as follows. Crystal precipitates are produced in the densification and grain growth stage (1200 °C peak temperature and 2-h dwell time). Crystal

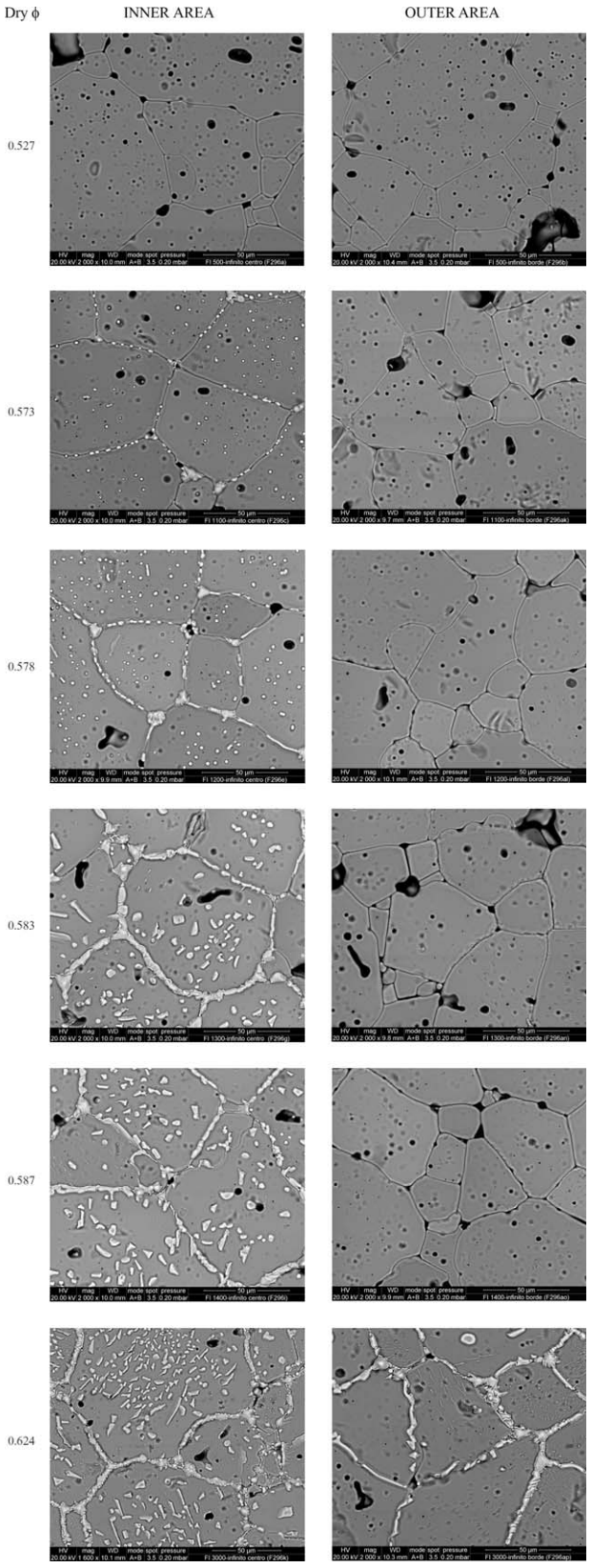

Fig. 1. Microstructure evolution of the tested dry relative densities (fast cooling).

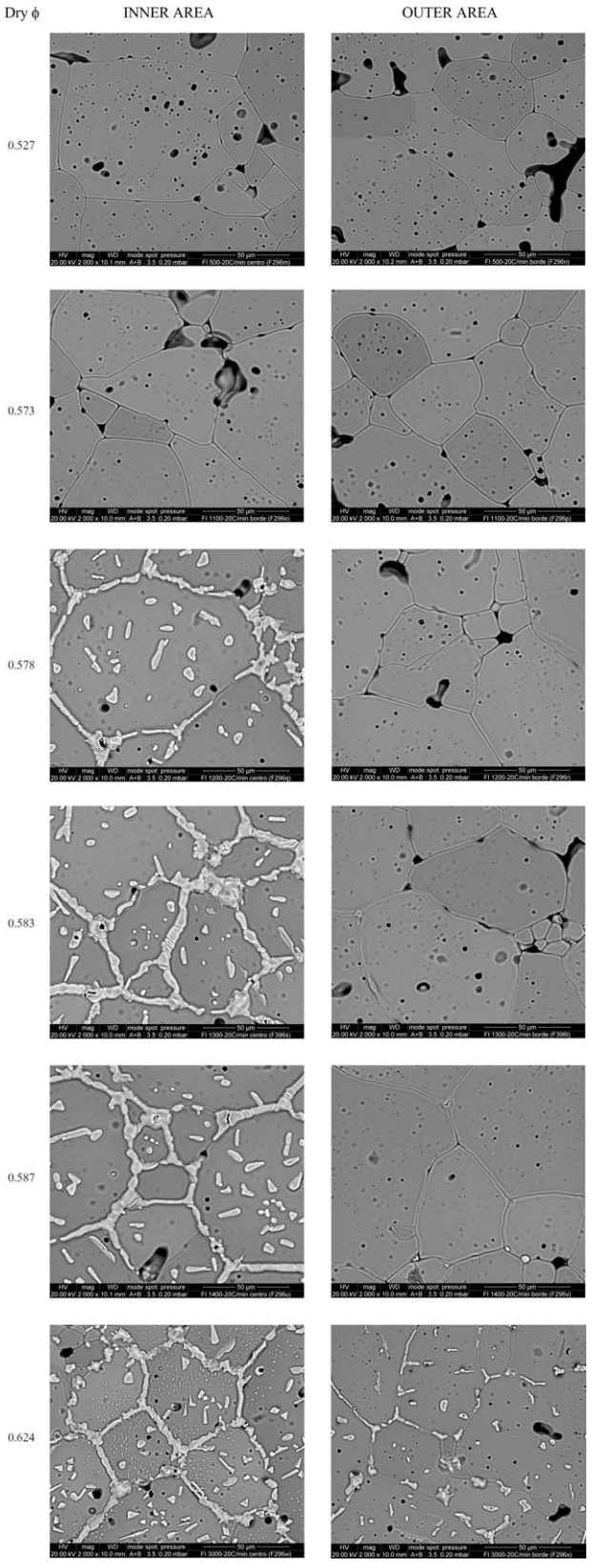

Fig. 2. Microstructure evolution of the tested dry relative densities (cooling at 20 °C/min).

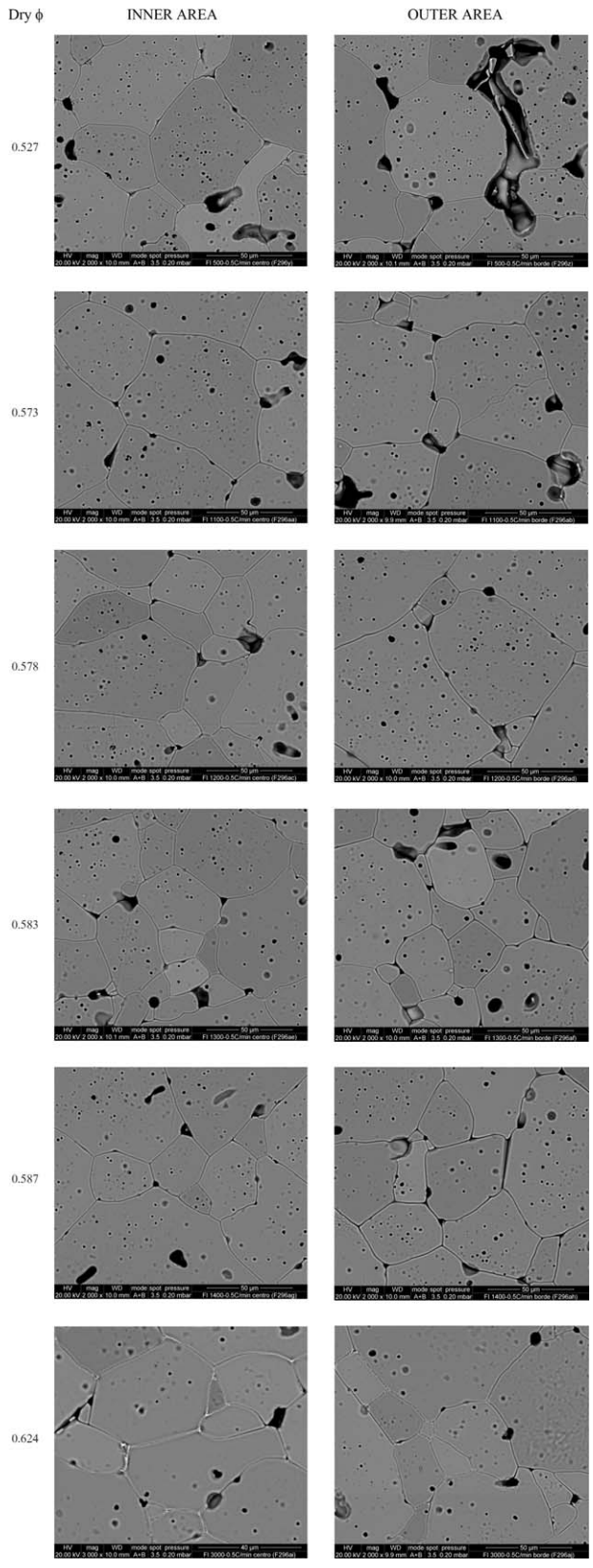

Fig. 3. Microstructure evolution of the tested dry relative densities (cooling at 0.5 °C/min).

precipitates dissolve in the ferrite grains during cooling (the lower the cooling rate, the higher the dissolution). Dissolution depends on oxygen concentration and sintered relative density (the process proceeds from the outer area inwards, because the oxygen comes from the air; the process occurs more readily when the dry relative density is lower, since the oxygen moves through the body by diffusion). In the studied bodies with a small dry relative density, when low cooling rates were used, no crystal precipitates appeared after the thermal cycle. Needle-shaped crystals were observed to dissolve before the rounded ones.

3.2. EDX, XRD, and XPS results

In order to identify the nature of the crystal precipitates detected by SEM, three experimental techniques were used:

3.2.1. Energy-dispersive X-ray (EDX) microanalysis

The microstructure and grain boundaries of a sintered specimen with crystal precipitates are shown in Fig. 5. Three different regions may be distinguished in this figure, which have been labelled as follows:

F: (grey) ferrite matrix.
Z: (light-coloured) rounded crystal precipitates located on the grain surface, on the grain boundaries, and at triple joint points.
C: needle-shaped crystal precipitates (lighter-coloured than the Z crystal precipitates) located on the grain surface and around Z crystal precipitates.

Table 2 details the semi-quantitative average chemical composition of two sintered specimens, without and with crystal precipitates, and also the semi-quantitative point chemical composition of the F area and the Z and C crystal precipitates, analysis being performed twice at high vacuum. The following may be observed:

1. The semi-quantitative average chemical composition of specimens without and with crystal precipitates was very similar to the chemical composition of the ferrite powder. In the case of the specimen with crystal precipitates, a small increase in the Zn peak was to be noted.
2. The semi-quantitative point chemical composition of the F area was also similar to the semi-quantitative average chemical composition of the specimen without crystal precipitates and to that of the ferrite powder.
3. The semi-quantitative point chemical composition of the Z crystal precipitates displayed a very significant increase in the Zn peak, while the semi-quantitative point chemical composition of the C crystal precipitates exhibited a very important rise in the Cu peak. These results suggest that the Z crystal precipitates were zinc oxide crystals, and the C crystal precipitates were copper oxide crystals.

3.2.2. X-ray diffraction (XRD) analysis

The sintered specimens were analysed by X-ray diffraction in order to determine the precipitate crystal structure.

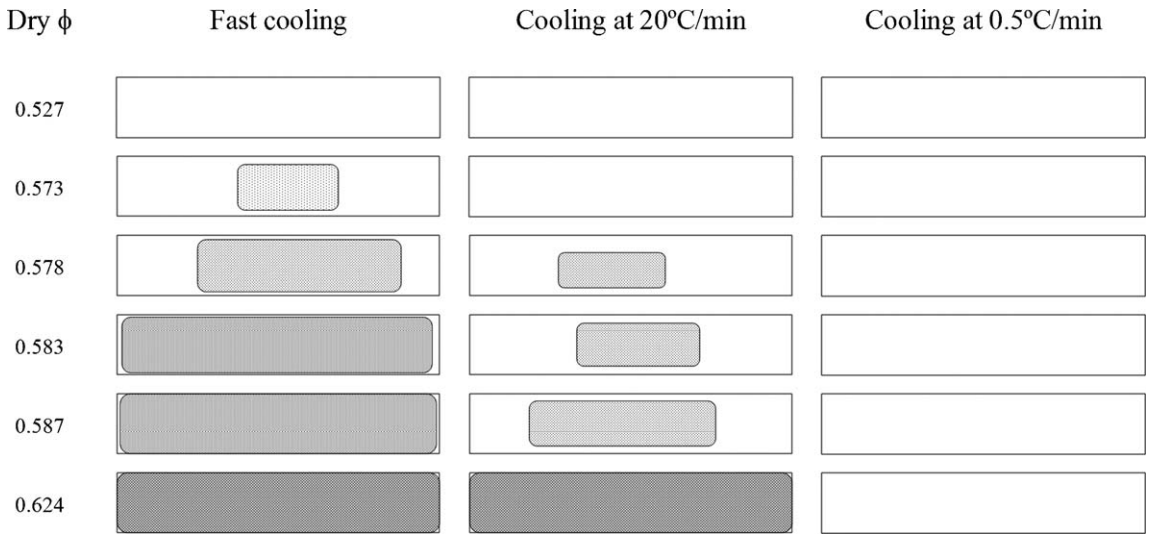

Fig. 4. Cross-sectional area occupied by crystal precipitates at the tested dry relative densities and cooling rates.

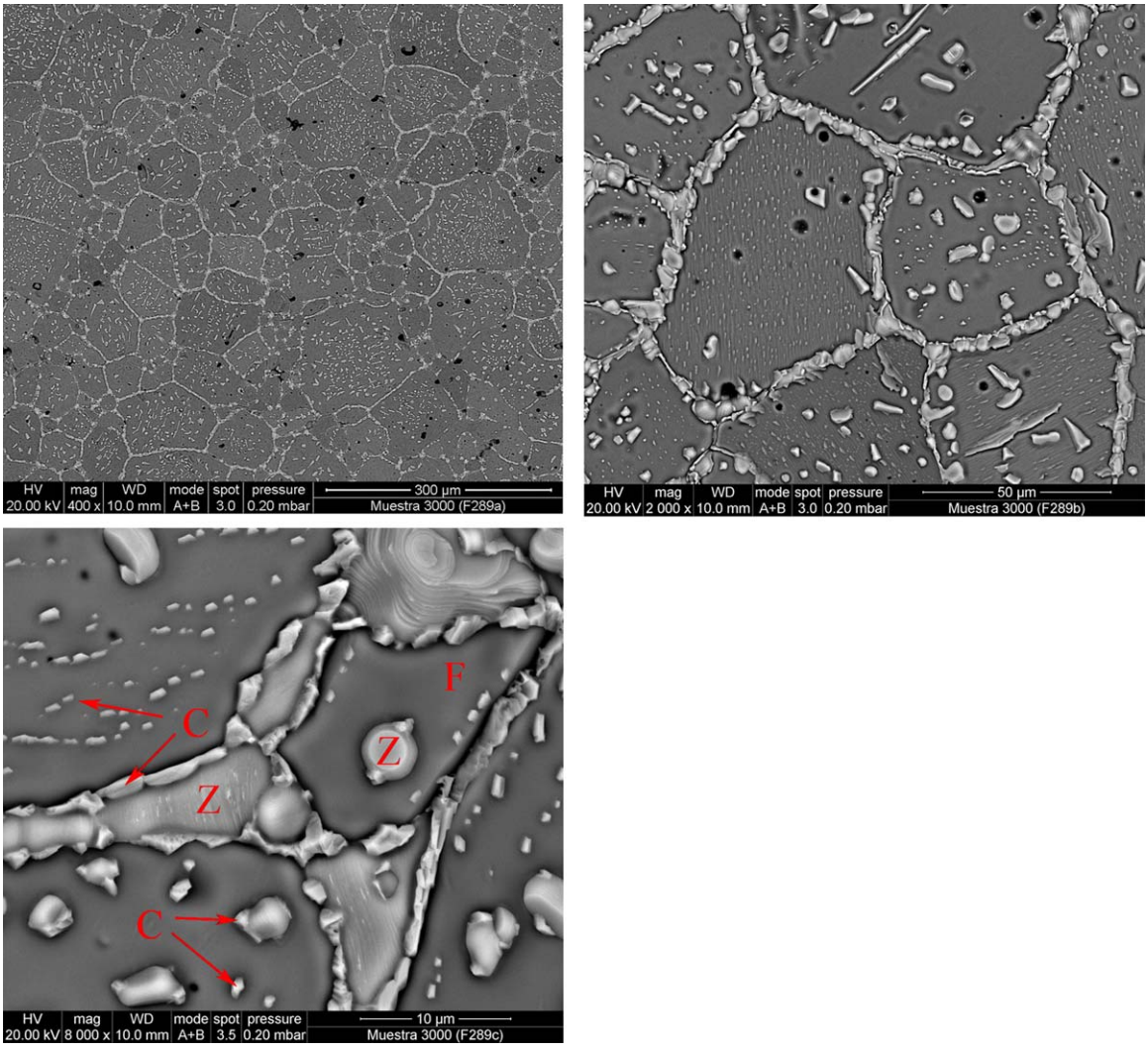

Fig. 5. Cross-sectional SEM micrograph showing the microstructure and grain boundaries of a sintered specimen with crystal precipitates.

Table 2
Semi-quantitative average chemical composition by EDX of two sintered specimens, without and with crystal precipitates, and semi-quantitative point chemical composition of the F area and Z and C crystal precipitates of a sintered specimen with crystal precipitates.

Chemical element	Specimen without crystal precipitates (mol%)	Specimen with crystal precipitates (mol%)	F area (mol%)		Z crystal precipitate (mol%)		C crystal precipitate (mol%)	
			1st analysis	2nd analysis	1st analysis	2nd analysis	1st analysis	2nd analysis
O	57.0	56.3	51.9	52.1	46.4	46.7	43.6	47.6
Fe	28.0	25.3	32.5	32.4	4.4	4.0	11.0	14.7
Ni	3.4	3.1	3.7	3.4	0.8	0.9	1.6	2.2
Zn	9.6	12.9	9.9	10.0	45.3	45.4	17.6	5.3
Cu	2.0	2.4	2.0	2.1	3.1	3.0	26.2	30.2

Table 3
Cross-sectional XPS analysis of two sintered specimen, without and with crystal precipitates (after 5 min sputtering).

Specimen	Cu (mol%)	Fe (mol%)	Ni (mol%)	O (mol%)	Zn (mol%)
Without crystal precipitates on cross-section	1.3	28.0	2.7	57.3	10.8
With crystal precipitates on cross-section	4.1	20.1	2.4	56.2	17.2

X-ray diffraction of the outer region of the sintered specimens, or of sintered specimens when they were milled to powder, exhibited franklinite (corresponding to the $ZnFe_2O_4$ ferrite) as sole crystalline phase. However, X-ray diffraction of the cross-sectional area of the rectangular etched surface (containing crystal precipitates) allowed two crystal structures to be identified: franklinite (corresponding to the $ZnFe_2O_4$ ferrite) and zincite (corresponding to ZnO). The zincite structure agreed with the EDX results of the Z crystal precipitates, which occurred particularly in the inner area. No crystal structure corresponding to the C crystal precipitates was identified, however, probably because the C crystal concentration was lower than the Z crystal concentration.

3.2.3. X-ray photoelectron spectroscopy (XPS) analysis

Table 3 shows the cross-sectional XPS analysis of two sintered specimens, without and with crystal precipitates (after 5 min sputtering). In the XPS spectra of the specimens (which include the Auger peaks) the higher intensity peaks, corresponding to Zn 2p, Zn LMM, Cu 2p, Ni 2p, Fe 2p, and O 1s, were chosen in order to try to differentiate the two specimens.

The area enclosed by each peak was quantified, taking into account the sensitivity factors proposed by the CasaXPS software for data treatment.[21,22] Table 3 again shows that the zinc and copper contents were higher in the specimen cross-section containing crystal precipitates than in that without the crystal precipitates.

The XPS spectrum of the specimen without crystal precipitates was considered to be representative of the binding energies of the chemical bonds in the ferrite structure at issue in this study. The differences between the XPS spectrum of the specimen without crystal precipitates and the XPS spectrum of the specimen with crystal precipitates (especially in the highest peaks) were thus presumably due to the occurrence of crystal precipitates. The following may be noted:

(a) In the case of the peaks corresponding to the Ni 2p and Fe 2p binding energies, there were no significant differences between the spectra, probably because Ni and Fe were only present in the ferrite structure and not in the crystal precipitates.
(b) In the case of the peak corresponding to Cu 2p binding energy, the binding energy corresponding to copper in the ferrite structure appeared in both spectra. However, the spectrum of the specimen with crystal precipitates also exhibited peaks corresponding to the Cu–O chemical bond in CuO (the typical shake-up may even be distinguished) and, probably, in Cu_2O. Fig. 6 and Table 4 show the deconvolution of the Cu 2p binding energy in the specimen with crystal precipitates, considering three contributions: copper in the ferrite, in the cupric oxide (CuO), and in the cuprous oxide (Cu_2O).
(c) The peak corresponding to Zn 2p binding energy (Fig. 7) displayed higher intensity in the specimen with crystal precipitates and was slightly shifted to the right (higher binding

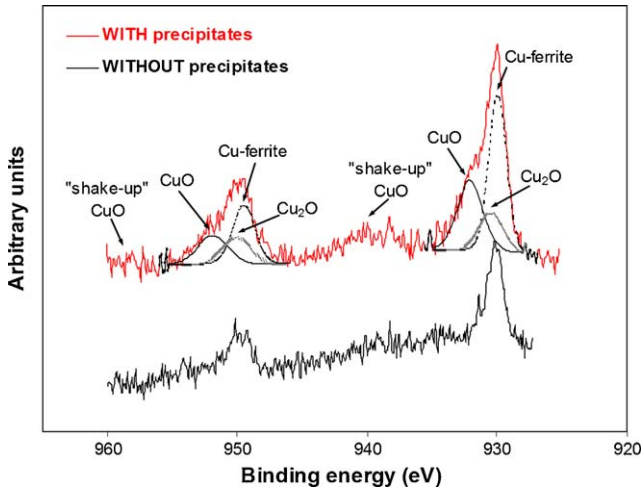

Fig. 6. Deconvolution of the Cu 2p XPS diagram of two sintered specimens, without and with crystal precipitates.

Table 4
Deconvolution of the Cu 2p XPS diagram of a sintered specimen with crystal precipitates.

Chemical element	Peak position (binding energy, eV)			mol%
	Cu $2p_{3/2}$	Cu $2p_{1/2}$	Energy difference	
Cu in ferrite	930.0	949.5	19.5	46.4
Cu in CuO	932.1	951.9	19.8	32.2
Cu in Cu_2O	930.5	950.1	19.8	21.4

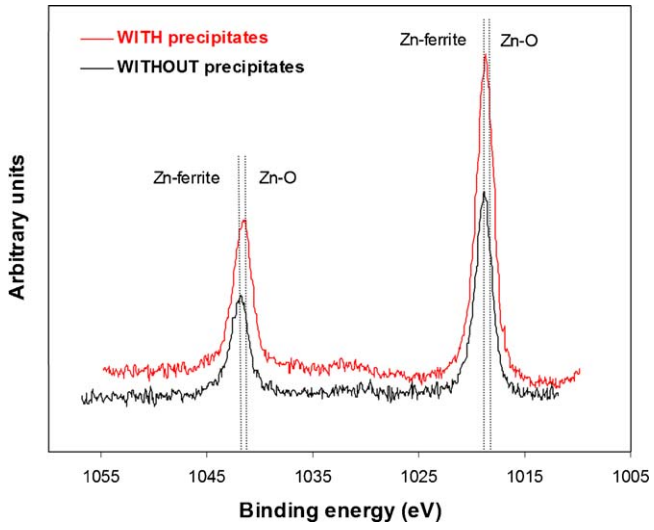

Fig. 7. Cross-sectional XPS analysis of two sintered specimens, without and with crystal precipitates, in the Zn 2p binding energy range.

energy), probably due to the occurrence of the Zn–O bond in the ferrite as well as in the zinc oxide. This result was more obvious in the Zn LMM kinetic energy range (Auger peaks) (Fig. 8). Table 5 shows the deconvolution of the Zn 2p binding energy in the specimen with crystal precipitates, considering two contributions: zinc in the ferrite and zinc in the zinc oxide (ZnO).

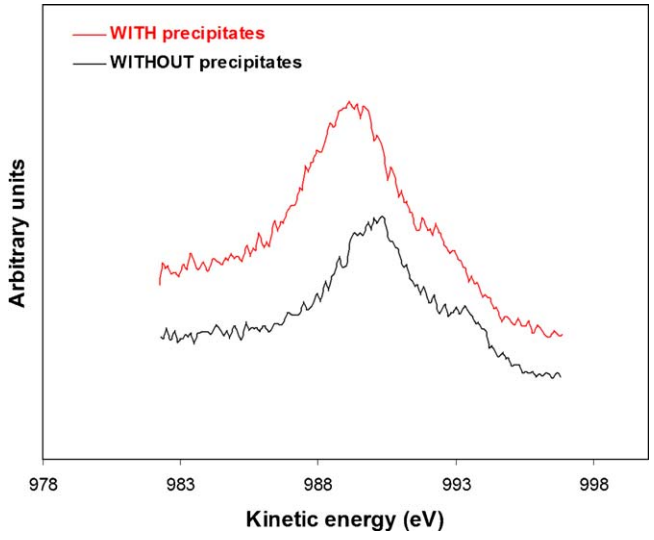

Fig. 8. Cross-sectional XPS analysis of two sintered specimens, without and with crystal precipitates, in the Zn LMM kinetic energy range.

Table 5
Deconvolution of the Zn 2p XPS diagram of a sintered specimen with crystal precipitates.

Chemical element	Peak position (binding energy, eV)			mol%
	Zn $2p_{3/2}$	Zn $2p_{1/2}$	Energy difference	
Zn in ferrite	1018.9	1042.0	23.1	38.9
Zn in ZnO	1018.7	1041.5	22.8	61.1

ZnLMM kinetic energy of the sintered specimen with crystal precipitates = 989.3 eV.
Auger parameter = BE (Zn $2p_{3/2}$) + KE (ZnLMM) = 1018.7 + 989.3 = 2007.95 eV → ZnO.

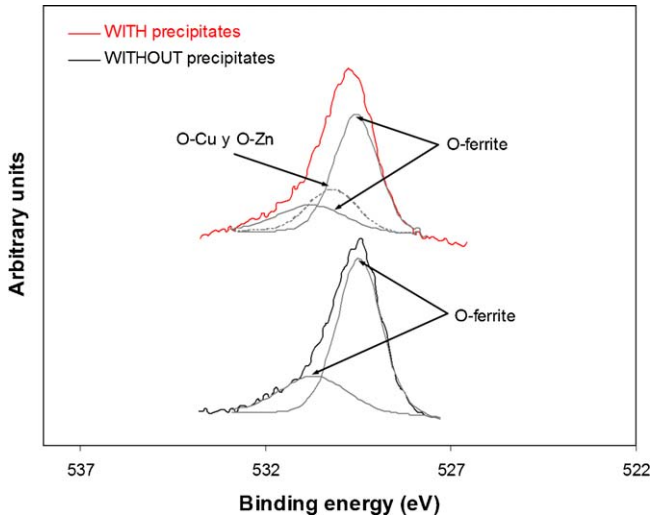

Fig. 9. Deconvolution of the O 1s XPS diagram of two sintered specimens, without and with crystal precipitates.

(d) The peak corresponding to O 1s binding energy shifted when crystal precipitates appeared. Fig. 9 shows the deconvolution of O 1s binding energy in the specimens without and with crystal precipitates, and Table 6 shows the deconvolution of O 1s binding energy in the specimen with crystal precipitates. Two contributions needed to be considered in the specimens without crystal precipitates to explain the two different (octahedral and tetrahedral) sites defined by the oxygen network. In the specimens with crystal precipitates, an additional contribution needed to be considered, which again confirmed the occurrence of copper and zinc oxides together in the ferrite structure.

The deconvoluted curves allowed the atomic compositions of the crystal precipitates to be estimated; these are given and compared with that of the ferrite composition in Table 7. In view of the position (binding energy) of the peaks used for deconvolu-

Table 6
Deconvolution of the O 1s XPS diagram of a sintered specimen with crystal precipitates.

Chemical element	Peak position (binding energy, eV)	mol%
O in crystal precipitates	530.3	22.6
O in ferrite	529.5 and 530.8	77.4

Table 7
Estimated atomic composition of the crystal precipitates from the deconvoluted XPS peaks.

Chemical element	Ferrite atomic composition (mol%)	Atomic composition of the crystal precipitates (mol%)
O	43.5	12.7
Fe	20.1	–
Zn	6.7	10.5
Ni	2.4	–
Cu	2.0	2.2

tion, the crystal precipitates probably contained ZnO, CuO, and Cu_2O. Zinc oxide may be estimated at about 24% (mass percentage), cupric oxide at about 3% (mass percentage), cuprous oxide at about 2% (mass percentage), and ferrite at about 71% (mass percentage).

3.3. Comments

Majima et al.[18–20] studied the microstructural changes that occurred during the sintering of Ni–Zn ferrites used as thin-film magnetic recording heads. They detected the presence of ZnO crystal precipitates on the grain boundaries, especially at the triple points, in samples sintered at 1180 °C. They noted no crystal precipitates in samples sintered in oxygen atmosphere, whereas samples sintered in air atmosphere contained crystal precipitates.

In preliminary laboratory experiments on Cu-doped Ni–Zn ferrites for the present study, the authors had already observed that small variations in ferrite chemical composition (less iron oxide and more zinc oxide in the raw materials mixture) gave rise to ZnO crystal precipitates during sintering. Fig. 10 shows the ternary phase diagram[23] of Fe_2O_3–ZnO–NiO. The line between

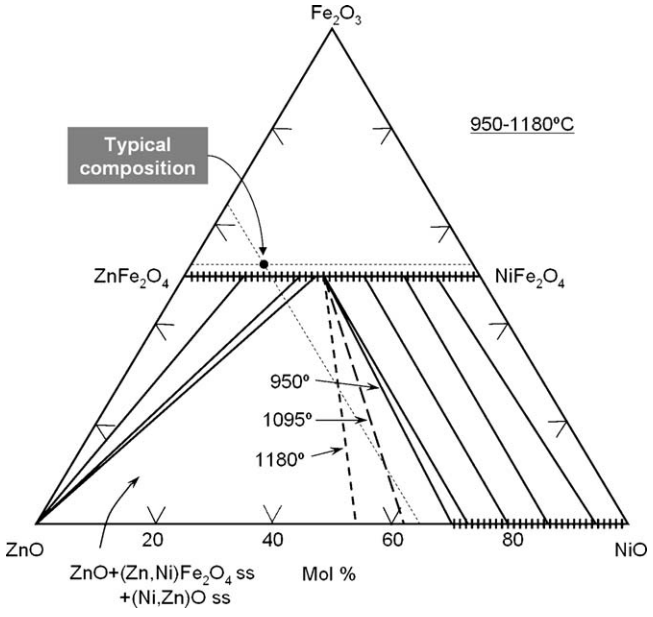

Fig. 10. NiO–ZnO–Fe_2O_3 phase diagram showing the typical ferrite chemical composition (black dot).

$ZnFe_2O_4$ and $NiFe_2O_4$ corresponds to the Ni–Zn ferrite composition. It may be observed that small variations in composition could lead to ZnO devitrification, which it would be possible to avoid in Ni–Zn ferrites by using a chemical composition that was slightly richer in iron with relation to the theoretical formula MFe_2O_4 (typical composition shown in Fig. 10). The corresponding quaternary phase diagram was not found in literature. However, the behaviour of the quaternary phase may be expected to resemble that of the Ni–Zn ferrites, and the ferrite composition may be expected to play a determining role in the possible devitrification of ZnO and certain other crystalline phases during sintering.

The experimental data in this paper show that, under certain conditions, crystal precipitates occurred when Cu-doped Ni–Zn ferrites were sintered. Cooling speed must have a marked influence on the occurrence of crystal precipitates, affecting the kinetics of the devitrification process. Analogously to the Majima studies,[18–20] oxygen concentration was also found to have a determining influence on the formation of crystal precipitates.

In the present study it was observed that specimens with a small dry relative density (high porosity – especially open porosity) contained no crystal precipitates after sintering; however, crystal precipitates occurred when dry relative density increased. Similarly, when the specimens were cooled at low speed after sintering, no crystals precipitated; however, when cooling speed increased, crystal precipitates occurred (Fig. 4). This is because higher dry relative density entails lower open porosity, leading to closed porosity in the first sintering stage. This closed porosity keeps the oxygen in the air from entering the pores. Similarly, low cooling rates allow oxygen to enter the pores for a longer time than fast cooling does. Porosity and cooling rate are, therefore, both determining factors with relation to the presence of oxygen inside the pores. This is consistent with the findings in this paper: the precipitation of ZnO and CuO (with a possible subsequent reduction of Cu(II) to Cu(I)) was strongly dependent on the oxygen concentration inside the pores. The following reactions would satisfactorily explain this dependence:

$$\begin{matrix}[Cu_{0.12}Ni_{0.23}Zn_{0.65}]Fe_2O_4(s) \\ \uparrow\downarrow \\ [Cu_{(0.12-x)}Ni_{0.23}Zn_{(0.65-y)}]Fe_2O_{(4-x-y)}(s) + xCuO(s) + yZnO(s)\end{matrix} \quad (1)$$

The quaternary phase diagram would explain the marked dependence of reaction (1) on composition and temperature (just as Fig. 10 explains this dependence in the case of Ni–Zn ferrites). Reaction (1) is consistent with the experimental data obtained in this study and with those reported in the literature.[18–20]

The CuO obtained in reaction (1) was unstable at high temperatures, as reported in the traditional chemical literature,[24,25] and decomposed as follows:

$$2CuO(s) \rightleftarrows Cu_2O(s) + \frac{1}{2}O_2(g) \quad (2)$$

the equilibrium constant being:

$$K_p = \sqrt{p_{O_2}}(atm^{1/2}) \quad (3)$$

Reactions (1) and (2) are consecutive, the latter affecting the equilibrium of the former. Ferrite decomposition according to reaction (1) could be minimized by controlling initial composition and sintering temperature. Reaction (2) would be less important if there was a gas phase with a higher oxygen content.

Consequently, the formation of zinc and copper oxide crystal precipitates could be due to the sintering process being faster than oxygen diffusion from outside into the pores. The absence of oxygen inside the pores leads to reactions (1) and (2), producing bulk precipitation of ZnO and CuO and transformation of CuO to Cu_2O. After sintering, in the cooling stage, reactions (1) and (2) could shift to the left, depending on the oxygen entering the pores. This process becomes more important when specimen porosity is high enough and/or cooling speed is low enough to allow oxygen diffusion in both cases, even though the diffusion coefficient is small. The net effect is re-dissolution of the crystal precipitates in the ferrite crystal structure, the process proceeding from the outer region inwards.

4. Conclusions

For a ferrite of composition $(Cu_{0.12}Ni_{0.23}Zn_{0.65})Fe_2O_4$, under the test conditions used, the study allows the following conclusions to be drawn:

1. During the heating stage, depending on the microstructure of the unfired specimens, rounded crystals as well as smaller elongated crystals can precipitate. The rounded crystals initially precipitated at triple points, then on grain boundaries and, subsequently, when the grain boundaries were saturated, inside the grains; the smaller elongated crystals precipitated around the former crystals.
2. The nature of the crystal precipitates was determined using energy-dispersive X-ray (EDX), X-ray diffraction (XRD), and X-ray photoelectron spectroscopy (XPS) analysis techniques: the rounded crystal precipitates were zinc oxide, while the smaller elongated crystals were copper oxides.
3. Two consecutive chemical reactions are put forward, which explain the bulk precipitation of the zinc and copper oxides in the specimen during sintering and their re-dissolution during cooling. In one of these chemical reactions, oxygen gas plays a key role, so that the degree of advance of this reaction (in both directions) largely depends on gas diffusion throughout the porous solid.

Acknowledgements

The study has been conducted with funding from the project MAT2008-05590, in the frame of the VIth Spanish National Plan for Scientific Research, Development, and Technology Innovation 2008–2011.

References

1. Kim KY, Kim WS, Ju YD, Jung HJ. Effect of addition of the CuO–Fe_2O_3 system on the electromagnetic wave absorbing properties of sintered ferrite. *J Mater Sci* 1992;**27**:4741–5.
2. Kim WS, Yoon SJ, Kim KY. Effects of sintering conditions of sintered Ni–Zn ferrites on properties of electromagnetic wave absorber. *Mater Lett* 1994;**19**(3–4):149–55.
3. Murthy SR. Low temperature sintering of NiCuZn ferrite and its electrical, magnetic and elastic properties. *J Mater Sci Lett* 2002;**21**(8): 657–60.
4. Kulikowski J, Lesniewski A. Properties of Ni–Zn ferrites for magnetic heads: technical possibilities and limitations. *J Magn Magn Mater* 1980;**19**:117–9.
5. Igarashi H, Okazaki K. Effects of porosity and grain size on the magnetic properties of NiZn ferrite. *J Am Ceram Soc* 1977;**60**(1–2): 51–4.
6. Bashkirov SH, Liberman AB, Khasanov AM. Effect of sintering temperature on crystalline and magnetic structure of nickel zinc ferrites. *Sov Powder Metall Met Ceram* 1988;**27**(5):367–70 [English translation].
7. Yan MF. Microstructural control in the processing of electronic ceramics. *Mater Sci Eng* 1981;**48**:53–72.
8. Sanyal J. Manufacture of ferrites. In: Kumar S, editor. *Handbook of ceramics: section B*. Calcutta: Kumar & Associates [s.a.]; 1995. p. 496–505.
9. Barba A, Orts MJ, Sánchez E, Clausell C. Kinetic model applicable to synthesis of $(Cu_{0.25}Ni_{0.25}Zn_{0.5})Fe_2O_4$ ferrite. *Br Ceram Trans* 2000;**99**(2):53–6.
10. Barba A, Clausell C, Felíu C, Monzó M. Influencia del tamaño de partícula, de la microestructura en crudo y del tratamiento térmico sobre la microestructura en cocido de una ferrita de Ni–Zn. In: *VIII Congreso Nacional de Materiales. Universidad Politécnica de Valencia, Valencia*. 2004. p. 317–24.
11. Barba A, Clausell C, Felíu C, Monzó M. Sintering of $(Cu_{0.25}Ni_{0.25}Zn_{0.50})Fe_2O_4$ ferrite. *J Am Ceram Soc* 2004;**87**(4):571–7.
12. Barba A, Clausell C, Monzó M, Cantavella V. Study of the sintering of ferrites of composition $(Cu_{0.25}Ni_{0.25}Zn_{0.50})Fe_2O_4$. In: *X Congreso Mediterráneo de Ingeniería Química: Ingeniería química y vida: abstracts. Fira de Barcelona, Barcelona*. 2005. p. 185.
13. Barba A, Clausell C, Monzó M, Cantavella V. Diseño del ciclo térmico de una ferrita, de composición $(Cu_{0.25}Ni_{0.25}Zn_{0.50})Fe_2O_4$, basado en su cinética de sinterización. In: Ramírez de Arellano A, et al., editors. *Innovación, ciencia y tecnología de los materiales cerámicos y vítreos 2005: Libro de resúmenes de los trabajos presentados a la XLV reunión anual de la Sociedad Española de Cerámica y Vidrio*. Sevilla: SECV; 2005.
14. Barba A, Clausell C, Monzó M, Jarque JC. Ciclo térmico para la obtención de una ferrita de Ni–Zn (I). Diseño de la etapa de sinterización. *Bol Soc Esp Ceram Vidr* 2008;**47**(1):13–23.
15. Barba A, Clausell C, Monzó M, Jarque JC. Ciclo térmico para la obtención de una ferrita de Ni–Zn (II). Influencia de la etapa de enfriamiento. *Bol Soc Esp Ceram Vidr* 2008;**47**(2):101–4.
16. Clausell C. *Sinterización en fase sólida de una ferrita de Cu, Ni, Zn: estudio de la cinética del proceso del desarrollo microestructural y de la permeabilidad magnética*. Tesis doctoral. Universitat Jaume I, Castellón; 2008.
17. Barba A, Clausell C, Felíu C, Monzó M, Nuño L, Heras D, Balbastre JV. Study of NiZn ferrite permeability: effect of relative density and microstructure. *J Am Ceram Soc* 2004;**87**(7):1314–8.
18. Majima K, Hasegawa M, Katsuyama S, Nagai H, Mishima S. ZnO precipitation during sintering of NiZn ferrite used for the substrate of thin-film heads. *J Mater Sci Lett* 1993;**12**:185–7.
19. Majima K, Hasegawa M, Yokota M, Mishima S, Nagai H. Microstructural control of Ni–Zn ferrites for thin film heads. *Mater Trans JIM* 1993;**34**(6):556–62.
20. Majima K, Hasegawa M, Katsuyama S, Mishima S, Nagai H. Influence of composition and oxygen partial pressure in sintering atmosphere on microstructure and magnetic properties of Ni–Zn ferrite for thin film magnetic recording heads. *Mater Trans JIM* 1995;**36**(11): 1392–7.
21. Wagner CD, Riggs WM, Davis LE, Moulder JF, Muilenberg GE. *Handbook of X-ray photoelectron spectroscopy*. Perkin-Elmer Corporation and Physical Electronics Division; 1979.

22. Moulder JF, Stickle WF, Sobol PE, Bomben KD. *NIST X-ray photoelectron spectroscopy database*. Minnesota, USA: Physical Electronics, Inc.; 1995.
23. Yamaguchi T, Takei T. Phase diagram and dissociation characteristics in the ferrite region of the system Zn–Fe–O in oxygen pressure of the atmosphere. *Sci Paper Inst Phys Chem Res* 1959;**53**(1517):207–15.
24. Cotton FA. *Advanced inorganic chemistry*. New York: John Wiley & Sons Corporation; 1999. pp. 856–867.
25. Massey AG, Thompson NR, Johnson BFG, Davis R. *The chemistry of copper, silver and gold*. Oxford: Pergamon Texts in Inorganic Chemistry; 1973.